nature physics

ARTICLES

PUBLISHED ONLINE: 2 FEBRUARY 2015 | DOI: 10.1038/NPHYS3211

Photon transport enhanced by transverse Anderson localization in disordered superlattices

P. Hsieh[1,2*], C. Chung[2,3], J. F. McMillan[1], M. Tsai[2,4], M. Lu[5], N. C. Panoiu[6,7*] and C. W. Wong[1,8*]

Controlling the flow of light at subwavelength scales provides access to functionalities such as negative or zero index of refraction, transformation optics, cloaking, metamaterials and slow light, but diffraction effects severely restrict our ability to control light on such scales. Here we report the photon transport and collimation enhanced by transverse Anderson localization in chip-scale dispersion-engineered anisotropic media. We demonstrate a photonic crystal superlattice structure in which diffraction is nearly completely arrested by cascaded resonant tunnelling through transverse guided resonances. By modifying the geometry of more than 4,000 scatterers in the superlattices we add structural disorder controllably and uncover the mechanism of disorder-induced transverse localization. Arrested spatial divergence is captured in the power-law scaling, along with exponential asymmetric mode profiles and enhanced collimation bandwidths for increasing disorder. With increasing disorder, we observe the crossover from cascaded guided resonances into the transverse localization regime, beyond both the ballistic and diffusive transport of photons.

In regular isotropic optical media the characteristics of dispersion relations, which among others define the properties of diffraction, are determined by the intrinsic structure of the medium so that there is little room to engineer the optical wave diffraction. By contrast, structuring the optical medium at the subwavelength scale can lead to marked changes of the characteristics of dispersion and wave diffraction. One such salient example is that of photonic crystals[1–9], whose wave dispersion and diffraction are engineered so as to achieve specific functionalities. Drawing an analogy to the transport of electrons in crystal solids, photonic crystals are recognized as providing insights into localization[10] in disordered and periodic scattering lattices. In particular, light localization in disordered media, including that of transverse localization in optically induced lattices[11], has been intensively investigated in the past[12–21]. For monochromatic electromagnetic propagation in an inhomogeneous and nondissipative dielectric medium, wave transport with a time-harmonic electric field amplitude $\mathbf{E}$ can be described by a Schrödinger-like equation:

$$-\nabla^2\mathbf{E}+\nabla(\nabla\cdot\mathbf{E})-\frac{\omega^2}{c^2}\varepsilon_{\mathrm{fluct}}(z)\mathbf{E}=\varepsilon_o\frac{\omega^2}{c^2}\mathbf{E} \qquad (1)$$

where the dielectric scattering potential fluctuations $\varepsilon_{\mathrm{fluct}}$ are distinct from the background (periodic) potential ε_o, such as in tight-binding models for disordered electronic transport. For electrons in the weak-disorder limit (root-mean-square potential fluctuations $V_{\mathrm{r.m.s.}}$ less than $\hbar^2/2m^*a_c^2$, where m^* is the effective mass and a_c the correlation length of the fluctuations), a Mott transition can occur[22]; in the strong-disorder limit ($V_{\mathrm{r.m.s.}}$ greater than $\hbar^2/2m^*a_c^2$), an Anderson transition[10] can occur for near-universal localization in real materials. Such localization transitions for photons are also possible with strong disorder, examined previously in the longitudinal on-axis propagating direction[23]. Furthering the electronics–photonics analogy, the scaling theory of localization (zero conductance Σ for long length scales in one and two dimensions, and the mobility edge in three dimensions) and a modified Ioffe–Regel criteria ($kl^*\approx 1$, where k is the Bloch wavevector and l^* the scattering mean free path) are also relevant in electromagnetic transport.

However, unlike electron transport, where localized bound states are in deep potential wells, photon localization is in an intermediate frequency band (between low-frequency Rayleigh extended states and high-frequency geometrical optics propagation) and at an energy higher than the highest potential wells[12,13]. As illustrated in equation (1), the electromagnetic field is also vectorial and has an additional polarization density term $\nabla\cdot\mathbf{E}$ that has no electronic analogue. Furthermore, working with photons, photonic lattices offer an unequivocal scaling test of localization in a static disorder potential, unhindered by many-body electron–electron and electron–phonon scattering, as one of the most accessible approaches to examine localization. Examples include the first observations of photon transverse localization in bulk photorefractive crystals[10], which, with the $\sim 5\times10^{-4}$ index contrast in the paraxial limit, can be described by $i(\partial A/\partial z)+1/2k\left(\partial^2A/\partial x^2+\partial^2A/\partial y^2\right)+(k_{\mathrm{T}}/n_o)\Delta n\ (x,y)\ A=0$, where $A(\mathbf{r})$ is the slowly varying envelope of the time-harmonic field and k_{T} the transverse wavevector. With strong index contrast ($\sim$2) on-chip, however, intensive direct numerical approaches using Maxwell's equations have to be performed, with recent computational models of the pseudogap spectral function and photon density of states $\rho(\omega)$ in vicinity of the band edge, for example, using Bloch-mode expansion approaches[24]. Coherent backscattering in localization has been examined numerically and experimentally[25], supporting the possibility of the scaling theory of localization on-chip. Guided resonances in superlattices have

[1]Optical Nanostructures Laboratory, Center for Integrated Science and Engineering, Solid-State Science and Engineering, Mechanical Engineering, Columbia University, New York, New York 10027, USA. [2]Quantumstone Research Inc., Taipei 114, Taiwan. [3]Center for Micro/Nano Science and Technology and Advanced Optoelectronic Technology Center, National Cheng Kung University, Tainan 701, Taiwan. [4]Center for Measurement Standards, Industrial Technology Research Institute, Hsinchu 300, Taiwan. [5]Center for Functional Nanomaterials, Brookhaven National Laboratory, Upton, New York 11973, USA. [6]Department of Electronic and Electrical Engineering, University College London, Torrington Place, London WC1E 7JE, UK. [7]Thomas Young Centre, London Centre for Nanotechnology, University College London, 17-19 Gordon Street, London WC1H 0AH, UK. [8]Mesoscopic Optics and Quantum Electronics Laboratory, University of California, Los Angeles, California 90095, USA. *e-mail: ph2285@columbia.edu; n.panoiu@ucl.ac.uk; cheewei.wong@ucla.edu

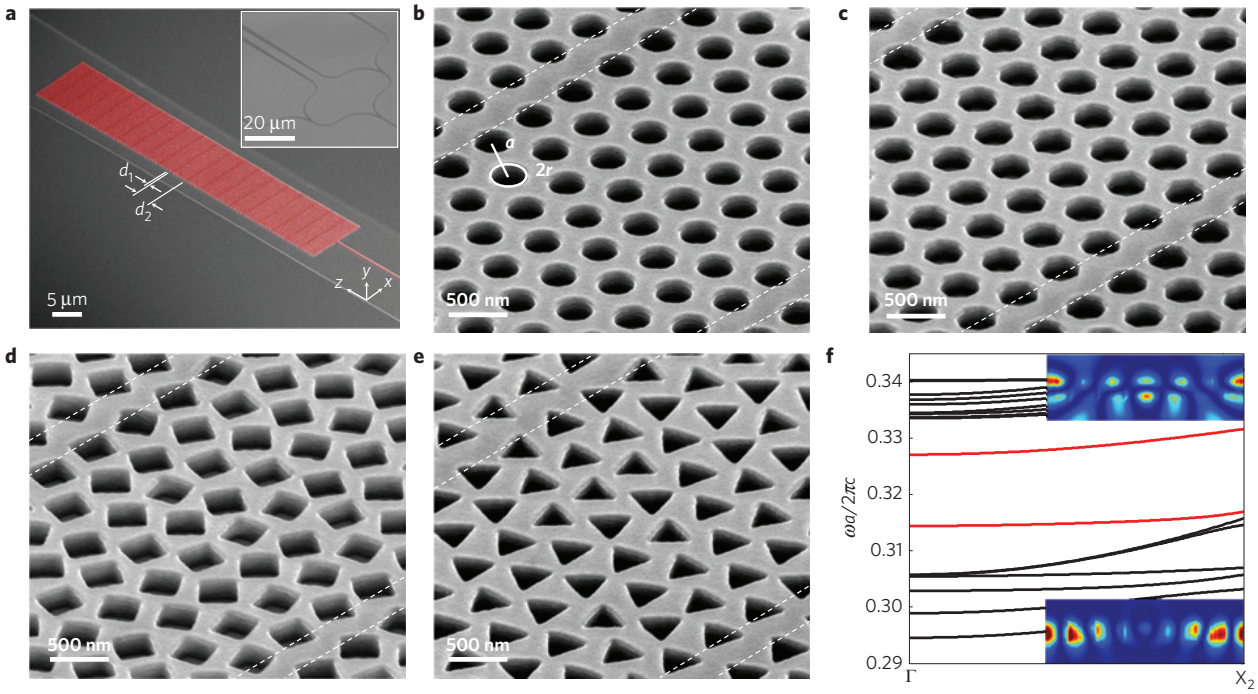

Figure 1 | Ordered and disordered superlattices. a, Example of nanofabricated silicon photonic superlattices with 20 superperiods and a single-mode input waveguide, imaged using a focused ion beam. Inset: on-chip input waveguide with a one-by-four splitter to four parallel superlattices for normalization. **b**, Ordered superlattices with circular holes. The dashed white lines depict the homogeneous region of the superlattices. **c**, Structural disorder is introduced by replacing the circular holes with heptagonal holes (approximately 2% structural disorder), and rotating them through an angle prescribed by a uniform random distribution. **d**, As **c** but with square holes (approximately 6% structural disorder). **e**, As **c** but with triangular holes (approximately 13% structural disorder). **f**, Band structure of the circular-hole superlattices, for the transverse wavevector component k_x. Inset: the flat bands (highlighted in red) near the normalized frequencies of approximately 0.314 and 0.327 correspond to two guided resonances excited in the transverse photonic crystal waveguides (top and bottom insets, respectively) with the computed $|E|^2$-profile plotted.

also been modelled numerically and observed experimentally[2]. In these high-index disordered superlattices, we demonstrate that the resulting transverse guided resonances, with disorder-induced inhomogeneous spectral broadening, can potentially provide improved collimation bandwidth while experiencing, within this frequency range, transverse localization.

Figure 1 shows the nanofabricated chip-scale anisotropic superlattices examined in our study, consisting of alternating layers of photonic crystal sections of thickness d_1, made of circular holes arranged in a two-dimensional hexagonal lattice with lattice constant $a = 500$ nm, and homogeneous sections of medium with thickness d_2 for a superperiod, $\Lambda = d_1 + d_2$. To introduce structural disorder, three other structures are also nanofabricated: heptagonal-hole superlattices (HHS; approximately 2% disorder), square-hole superlattices (SHS; approximately 6% disorder) and triangular-hole superlattices (THS; approximately 13% disorder). In each of these superlattices, disorder is introduced by randomly rotating each scatterer with a stochastically uniform distribution of the rotation angle. All devices are fabricated in silicon-on-insulator (Methods), with 20 superperiods, and the incoming transverse-magnetic-like (TM-like) polarized light is coupled into the superlattices by a single-mode waveguide of width $w = 450$ nm.

The thickness of the homogeneous section satisfies the relation $d_2/d_1 = 0.18$, with the superlattice band structures, computed along the Γ–X_2 direction of the superlattice, shown in Fig. 1f and Supplementary Information I. Significantly, as the superlattice band structure suggests, our photonic structure possesses nearly flat bands (highlighted in red) at the normalized frequencies of 0.314 and 0.327 (in dimensionless units of $\omega a/2\pi c$; centred around 0.322) at $k_x = 0$, corresponding to the high-symmetry Γ point. These flat bands represent leaky guided resonances (located outside the light cone)[3], which propagate transversely in the one-dimensional (1D) homogeneous dielectric region that forms a 1D photonic crystal waveguide (in dashed white lines in Fig. 1b–e) separating the photonic crystal sections of the superlattices. The underlying mechanism that leads to enhanced collimation in these superlattices is as follows: mutual coupling of the two leaky guided resonances excited at the input and output interfaces of a homogeneous section gives rise to the mode splitting seen in the red-highlighted bands of Fig. 1f. The $|E|^2$-field profiles of these resonances are shown in the insets of Fig. 1f. Bloch modes of the photonic crystal couple to these guided resonances and are resonantly amplified when tunnelling from one photonic crystal section to the next. This mechanism of resonant wave tunnelling via excitation of guided resonances enhances the diffraction-free beam collimation because the evanescent part of the optical field is propagated through the superlattice as well. This beam collimation mechanism based on resonant tunnelling—from guided resonances to guided resonances—is markedly different from that investigated in earlier studies[6–8], in which case the beam divergence is reduced by designing flat spatial dispersion surfaces or by alternating metamaterials layers of normal and anomalous dispersion (see Supplementary Information I to III for detailed design of the superlattices).

To quantify the degree of beam collimation, in Fig. 2 we show the computed effective beam width, $\omega_{\mathrm{effc}} = P^{-1}$, defined as the inverse participation ratio, $P(z) \equiv [\int I(x,z)^2 \mathrm{d}x]/[\int I(x,z)\mathrm{d}x]^2$ (ref. 10), where $I(x,z)$ is the field intensity. In these calculations we employed 3D finite-difference time-domain (FDTD) simulations (see Methods and Supplementary Information IV) performed across the 1,500 nm to 1,600 nm spectral domain with 5 nm

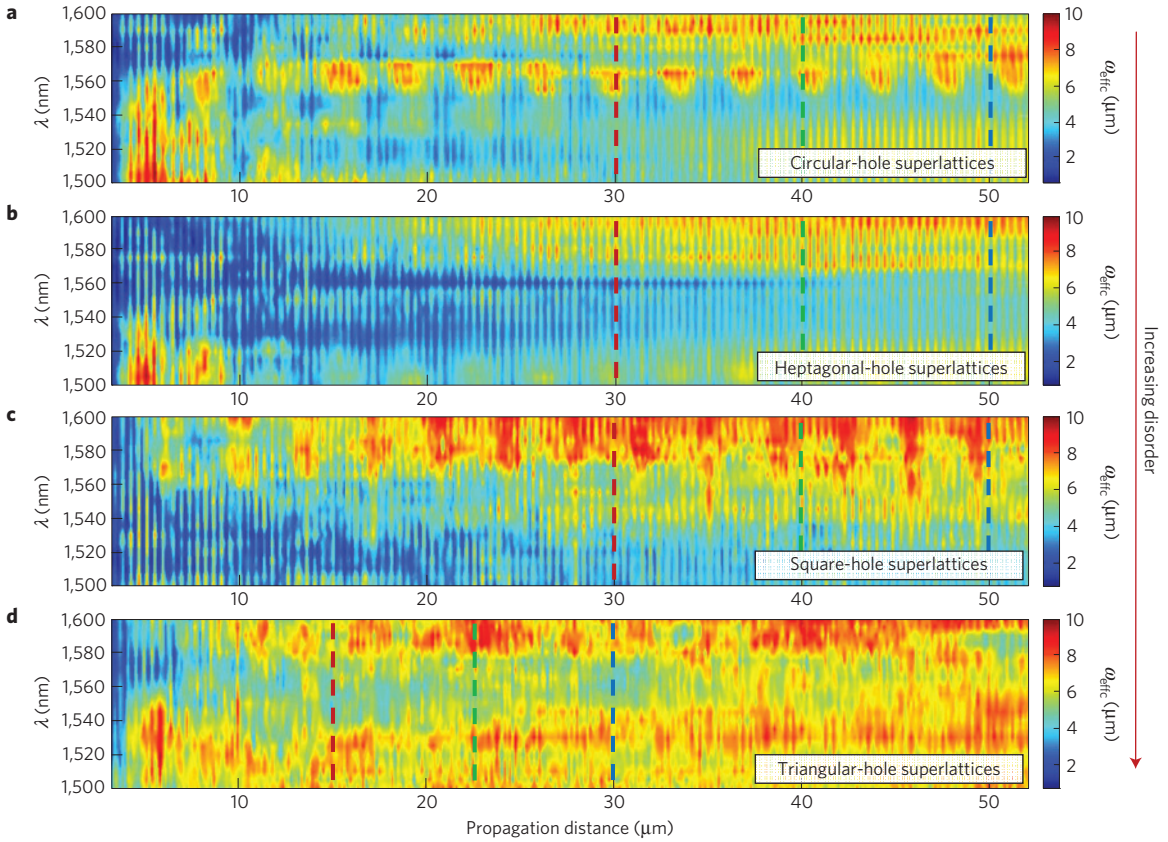

Figure 2 | Numerical dispersive-propagation maps for the ordered and disordered superlattices. a–d, The plotted effective beam width (blue shows the tightest spatial extent and red the widest) is determined from the near-field spatial distribution of the field intensity, computed from 3D finite-difference time-domain numerical simulations. For the circular-hole superlattices (**a**), collimation is observed to be centred at 1,550 nm. The heptagonal-hole (**b**), square-hole (**c**) and triangular-hole (**d**) superlattices show larger collimation bandwidths compared to the circular-hole superlattices. Input beam width is 450 nm. The coloured vertical dashed lines indicate the cross-sections of the dispersive propagation shown in Fig. 3.

resolution. The blue regions in Fig. 2 indicate the regions of tightest collimation; for our designed circular-hole superlattices (CHS), the collimation band is centred at 1,550 nm. With increasing disorder, the heptagonal-hole superlattices (HHS), Square-hole superlattices (SHS) and Triangular-hole superlattices (THS) structures show significantly larger bandwidths for collimation than does the CHS, as shown in Fig. 3. This is attributed to the inhomogeneous spectral broadening of the guided resonances induced by disorder. The frequency of the guided resonances at the Γ point is shifted by a random amount owing to the coupling of the optical mode with the adjacent, randomly perturbed photonic crystal sections of the superlattices[24], an effect that is also accompanied by increased radiation losses. Because the frequency dispersion of these tunnelling channels increases with disorder, the enhanced collimation bandwidth increases with disorder level as well. We note that in the instance of the rotated SHS the spectral region of strong collimation is slightly blueshifted with respect to the CHS owing to the fact that, even if the hole area is kept the same, the frequency dispersion of the guided resonances depends weakly on the hole shape.

Encouraged by these theoretical predictions, we examined the far-field infrared scattering for 900 wavelengths (1,530 nm to 1,620 nm with 100 pm spectral resolution), for each of the superlattices. Figure 4a highlights the key features, with further supporting examples shown in Supplementary Information V. For the CHS, the most effective collimation is observed at 1,550 nm (λ_{ec}), with the beam width at the interfaces, $\omega_{FWHM,i}$, fluctuating by less than ±7%. This wavelength is closest to that of the guided resonances, allowing more effective coupling, with larger tunnelling transmission and amplification of the evanescent part of the field. This is supported by the spectral analysis of the spatial full-width at half-maximum (FWHM), ω_{FWHM}, with the smallest beam width observed at λ_{ec} and matching well with the numerical simulation data, where the strongest collimation occurs in the region of $\lambda_{ec}-4$ to $\lambda_{ec}+4$ nm.

Figure 4a also shows the electromagnetic propagation for the disordered HHS, SHS and THS cases at the corresponding λ_{ec} wavelengths, compiled from 2,700 scattering images. Collimation is observed even in these disordered superlattices. The most effective λ_{ec} wavelengths are determined to be approximately 1,550 nm (HHS), 1,555 nm (SHS) and 1,580 nm (THS), respectively. At other wavelengths, the beam diverges significantly from its input excitation width in the disordered superlattices. Concurrently, the larger-disorder superlattices, such as the triangular and square realizations, show shorter transmission lengths owing to the increased disorder scattering losses from the perturbed Bloch modes. To observe finer features in the z-direction, we next perform near-field scanning optical microscopy (NSOM) at the λ_{ec} wavelengths to probe the local field intensity oscillations in each superlattice (see Supplementary Information VI). Mapping the near-field intensity with the superimposed photonic crystal topography, the periodic enhancement of the wave scattering is determined to be centred at the location of the transverse waveguides. These near-field measurements (calibrated with a periodic topography grid) also show the z-thin, x-long scattering slices corresponding to the thin homogeneous transverse waveguides. With increasing disorder, the near-field intensities at the interfaces become increasingly apparent compared to the background stray light (see Supplementary Fig. 13) owing to

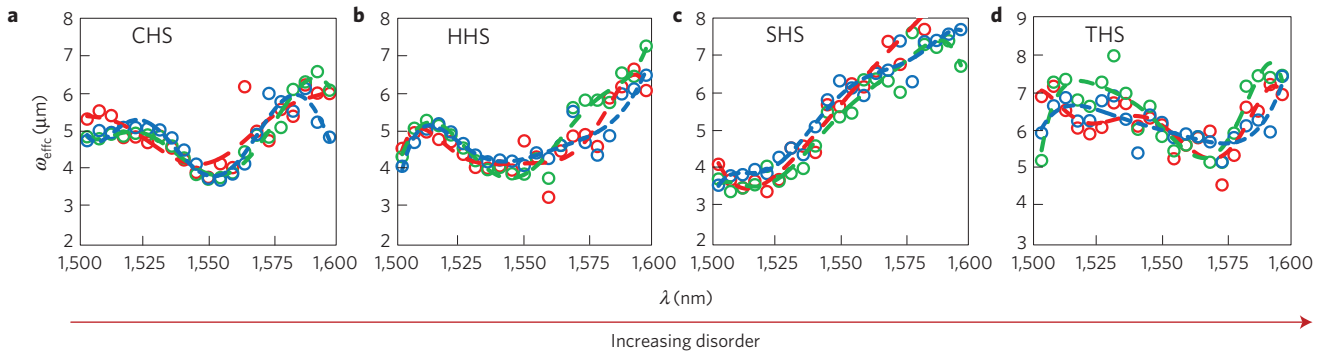

Figure 3 | Dispersive propagation of the ordered and disordered superlattices. a–d, The distribution of effective beam width versus wavelength at selected positions (indicated by the correspondingly coloured dashed vertical lines in Fig. 2), for the circular-hole (**a**), heptagonal-hole (**b**), square-hole (**c**) and triangular-hole (**d**) superlattices, exhibiting a flatter spectral response with increasing disorder. Each coloured dashed curve is a fit to the corresponding data points.

the increased scattering into the radiation continuum and the more efficient excitation of the guided modes.

To compare against the guided resonances approach, we next designed photonic crystals with sizes of a few hundred micrometres[6–8], but without the superlattices and with flat equifrequency dispersion curves. We nanofabricated and examined, under the same conditions, collimation in these lattices, as detailed in Supplementary Information VII. Figure 4b shows the observed beam propagation at λ_{ec} in the presence of disorder, in the collimation regime. The field profiles in Fig. 4b clearly demonstrate that in this case beam collimation is of a markedly different nature, as it almost completely vanishes in the presence of disorder. The averaged collimating beam width increases from approximately 2.2 μm to approximately 2.5 μm (heptagon hole), 6.8 μm (square hole) and 13.9 μm (triangular hole), without the guided resonance contributions. The fluctuation of the beam width increases from ±5% to ±6% (heptagon hole), ±9% (square hole) and ±11% (triangular hole).

Figure 5 shows the optical wave transport in the superlattices at different wavelengths, for different disorder. The physical nature of the electromagnetic propagation is revealed by the slope of the function $\omega_{FWHM}(z)$ when represented on a log–log scale. As shown in the log–log plots of Fig. 6a to d, the asymptotic dependence of the experimental effective ω_{FWHM} is of the form $\omega_{FWHM}(z) \propto z^{\nu}$, where the slope ν is a power exponent determined by linear fitting. For the CHS in Fig. 6a, we observe ν values up to 0.24 at the longer wavelengths, but with a near-zero slope $\nu \approx 0.05$ between $\lambda_{ec} - 4$ to $\lambda_{ec} + 4$ nm. This corresponds to an approximately 8 nm collimation bandwidth and is due solely to the beam interaction with the guided resonances. In the presence of roughly 2% and 6% structural disorder (HHS and SHS, respectively), however, the measured log–log plots of $\omega_{FWHM}(z)$ show a markedly different spectral dependence. The slope ν decreases significantly in the HHS between $\lambda_{ec} - 4$ and $\lambda_{ec} + 17$ nm, and in the SHS between $\lambda_{ec} - 4$ and $\lambda_{ec} + 17$ nm. This is shown in Figs 6b and c, respectively. In both superlattices a near-zero ν value of ≈0.05 is now achieved within a 21 nm collimation bandwidth, sizably larger than in the CHS.

The observed increased collimation arises from the disorder-induced inhomogeneous spectral broadening of guided resonances. To further support this, we next examined the THS structure, with larger (approximately 13%) structural disorder. The analysed experimental collimation bandwidth is even larger, namely approximately 31 nm ($\lambda_{ec} - 7$ to $\lambda_{ec} + 24$ nm), as shown in Fig. 6d. These observed near-zero ν bandwidths are also larger than (and outside) the bandwidth of the computed regular CHS without disorder, with an approximately 3.9 times increase in collimation bandwidth achieved experimentally in the presence of disorder as compared to the periodic disorder-free CHS. We also note that, to characterize the effects of disorder, an ensemble average is needed over different realizations of disorder; in our superlattices the ensemble average is self-consistently performed as the beam propagates over 20 disordered photonic crystal sections of the superlattices—each of the supercells having the same level of randomness but a different disorder realization. Furthermore, in the numerical modelling results, we note that in the high-index physical setting studied here we described the optical beam propagation with the 3D vectorial Maxwell's equations instead of a Schrödinger-type equation to account for the wave dynamics. The measured bandwidth increase of nearly zero ν with increasing disorder is also supported by our 3D simulations, both in terms of the general wavelength dependence of ν and its estimated bandwidth from disorder. We note the localization bandwidth computation is a higher-order analysis, especially with the disorder lattice models of ∼4,000 or more scattering sites, where there are slight deviations between the exact numerical and experimental lattice instances, and with the experimental samples containing additional disorder sources (such as from the sidewall roughness) that can account for the measured larger bandwidths.

This phenomenon of disorder-induced enhanced beam collimation is reminiscent of transverse localization. In isotropic media, ballistic transport is characterized with $\nu = 1$ and diffusive transport is characterized with $\nu = 1/2$; our measurements and simulations clearly demonstrate that the photon transport is arrested by disorder with ν values predominantly less than 0.05 in our disordered superlattices, even exceeding that of circular regular lattices. For the largest disorder (THS), we observed the strongest localization with consistently near-zero ν values, averaged at 0.017, and with an almost flat spectral dependence of ν. In this regime for all disordered superlattices, the beam is localized and its divergence is arrested by the structural disorder in the superlattices, subjected only to statistical fluctuations in the scattering sites. The observed transverse localization arises from multiple coherent scattering of light induced by the disordered potential, forming localized guided resonances at the homogeneous–photonic crystal interfaces. We also note that fluctuations in ω_{FWHM} increase with disorder (images in Supplementary Information V) and are consequently inversely proportional to the dimensionless conductance Σ_o ($\Sigma_o \approx \rho(\omega) D_o l^*$, with the diffusion coefficient D_o approximately equal to the power exponent slope ν). This reduced dimensionless conductance for increasing disorder arises owing to coherent backscattering in the guided resonances over macroscopic length scales.

We further confirm the transverse localization through an analysis of the transverse intensity beam profile and its z-axis spatial progression. This is performed by examining the transverse intensity profile fitted to an exponentially decaying form $I \sim \exp(-2|x|/\xi)$,

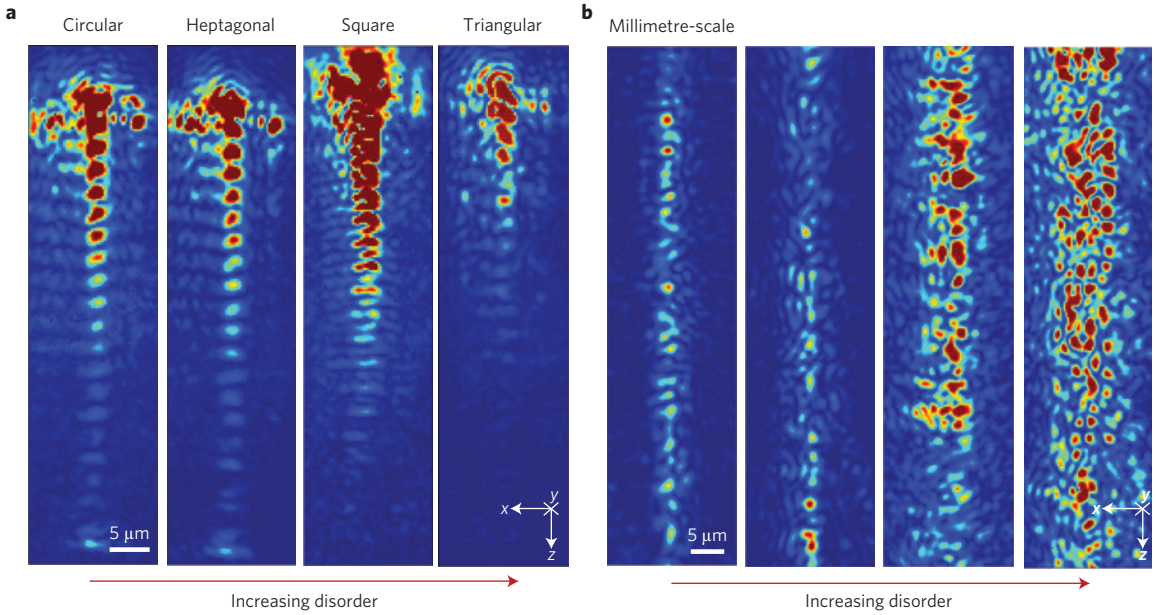

Figure 4 | High-resolution far-field infrared scattering images illustrating photon transport in the disordered superlattices. a, Circular-hole, heptagonal-hole, square-hole and triangular-hole superlattices at the λ_{ec} wavelengths. **b**, Disorder media without superlattices and with a collimation mechanism solely from flat spatial dispersion surfaces. Measurements are shown at the λ_{ec} wavelengths in the presence of disorder. Beam widths in these media with scales of a few hundred micrometres increase with increasing disorder, contrary to the superlattices.

where ξ is the localization length (the exponential decay length of the confined modes and defined with $l^* \exp(\pi k_T l^*/2)$, a characteristic length scale of Anderson localization). For instance, in the case of HHS investigated at $\lambda_{ec} + 17$ nm, our analysis shows that ξ is 25 μm for the $z = 25$ μm location and it roughly preserves an exponential transverse profile (instead of a Gaussian profile, as is the case for diffusive transport). We also note that the beam profile becomes increasingly more asymmetric as disorder increases (as detailed in the Supplementary Information V and Supplementary Fig. 12). The exponential profile is also found to be the best fit for the SHS and THS cases. The exponential profile is a clear indication of chip-scale localization, with wave interference from the interplay of disorder on the periodic lattice.

For the circular superlattices without appreciable disorder, a new type of anisotropic medium based on cascaded excitation of guided resonances is observed, with highly dispersive features and supported by both experimental measurements and numerical modelling. With increasing disorder, beam collimation in heptagonal, square and triangular superlattices are observed for the first time. With increasing disorder strength, we observed increased collimation bandwidth, tighter collimation than in regular circular superlattices, and enhanced transverse localization. Transport in disordered superlattices reaches a regime of almost arrested diffraction, departing significantly from diffusive and ballistic transport, a phenomenon verified by the power-law scaling of the beam width and exponentially decaying asymmetric intensity beam profiles in the localization regimes.

The observed transverse Anderson localization allows us to access values of the collimation bandwidth that are difficult to access through other approaches. By analogy to electronic transport, these observations allow us a means to probe the transverse Anderson localization of photons in solid-state semiconductors, including the role of guided resonances and the localization evolution. Future studies include optical nonlinearity perturbations to the localization (for different disorder levels) with potential spontaneous pattern formation, background scattering potentials with quasicrystal geometries, or the probing of these spatially localized modes with entangled biphoton states. The optical

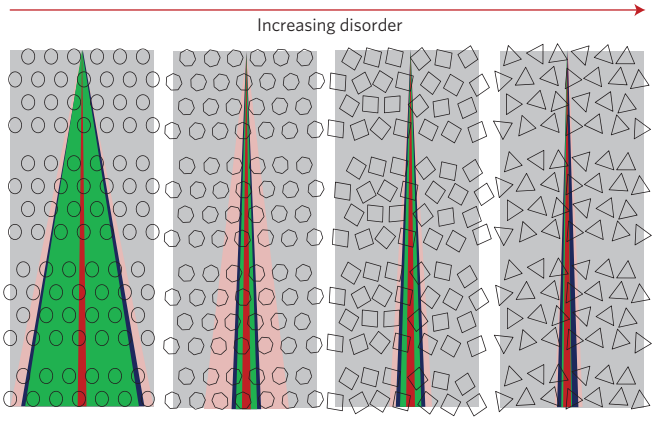

Figure 5 | Disorder-induced enhanced photon transport at the onset of transverse localization. Schematic of infrared scattering for superlattices with different disorder (from left to right): circular, heptagonal, square and triangular scatterers. The colour plots correspond to the different wavelengths shown in the other panels. The beam diverges in the circular-hole superlattices but shows collimation in the heptagonal-hole and square-hole superlattices.

measurements developed here can find applications to other areas of physics as well. For example, photon transport in our superlattices is in many aspects analogous to electron wave dynamics in graphene heterostructures[26], so that similar effects could be observed in electron transport in a superlattice of closely spaced disordered graphene nanoribbons[27]. The role of the guided resonances in this system arises from the nanoribbon edge states. These same phenomena could also be explored in other studied electronic systems, such as semiconductor superlattices[28] and oxide heterojunctions[29], with interface states playing the role of guided resonances. Matter-wave transport in atomic[30,31] and polariton[32] Bose–Einstein condensates trapped in suitably designed optical superlattices could also provide fertile testing grounds of the conclusions of our work.

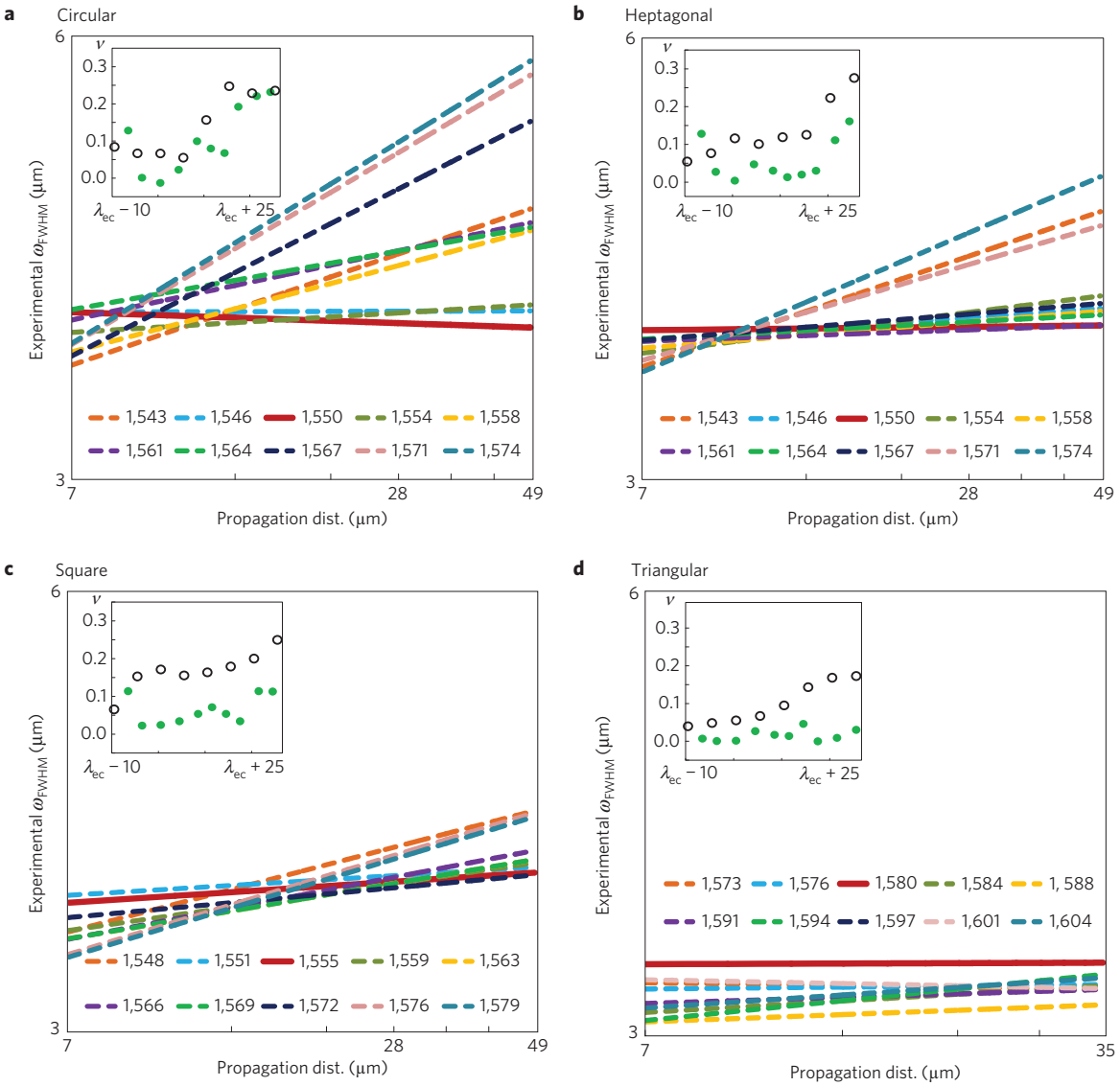

Figure 6 | Photon transport enhanced by transverse localization. a–d, Log–log plots of the experimentally derived effective beam width $\omega_{FWHM}(z)$ versus propagation distance for circular-hole (**a**), heptagonal-hole (**b**), square-hole (**c**) and triangular-hole (**d**) superlattices, determined from the full-width at half-maximum of the far-field infrared scattering, in the spectral region $\lambda_{ec}-4$ to $\lambda_{ec}+24$ nm. The red solid lines represent the approximate wavelength for most effective collimation λ_{ec} (with least beam divergence; see also Supplementary Information V). Inset: distributions of the slope ν in the spectral region $\lambda_{ec}-10$ to $\lambda_{ec}+25$ nm. The green filled dots and black open circles, respectively, represent the experimental and numerical simulation values of ν.

Methods

Device nanofabrication. The photonic crystal structures shown in Fig. 1 were fabricated on a silicon-on-insulator wafer with a single-crystal silicon slab ($n_{si}=3.48$) of 320 nm thickness on top of a 2 μm-thick layer of buried oxide ($n_{SiO_2}=1.46$), with electron-beam lithography. ZEP520A (100%) resist was spin-coated at 4,000 revolutions per minute for 45 s to a thickness of ≈350 nm, then baked at 180 °C for 3 min. The JEOL JBX6300FS electron-beam lithography systems at Brookhaven National Laboratory-USA and ELIONIX ELS7500EX at National Cheng Kung University-Taiwan, respectively, were used to expose the ZEP520A resist to define the pattern, followed by development in amyl acetate for 90 s and rinsing with isopropyl alcohol (IPA) for 45 s to completely remove any residue of amyl acetate developer.

An Oxford Instruments Plasmalab 100 was used for pattern transfer onto the silicon layer of the silicon-on-insulator wafer, using an inductively coupled plasma reactive ion etcher (ICP-RIE) to perform the cryogenic silicon etching. O_2 at −100 °C was applied in the chamber first for cleaning and cooling, followed by cryogenic etching at −100 °C using a mixture of SF_6 (40 sccm) and O_2 (15 sccm) at 15 W radiofrequency (r.f.) power, 800 W ICP power and 12 mtorr pressure for a total of 16 s. The resulting wafer was subsequently placed in a *n*-methyl pyrrolidone (NMP 1165) resist remover for about 4 h to completely remove the remaining ZEP resist.

Band structure and time-domain numerical simulations. The band diagrams of the photonic crystals and photonic superlattice are computed with the RSoft software BandSOLVE, a commercially available software that implements a plane wave expansion algorithm. In all numerical simulations a convergence tolerance of 10^{-8} was used to compute the frequency bands. The photonic bands of the photonic crystal have been divided into TM-like and TE-like polarizations, according to their parity symmetry. The effective refractive indices corresponding to the TM-like bands are determined from the relation $k=\omega|n|/c$, with k in the first Brillouin zone (see Supplementary Information).

The numerical simulations of the intensity field distribution were performed by using the MIT code MEEP, a freely available code based on the finite-difference time-domain (FDTD) method. In all numerical simulations we used a uniform computational grid with 33 grid points per micrometre. This ensures that the smallest characteristic length of the system (in our case, the hole diameter) is sampled by at least ten grid points. In our FDTD simulations we used a continuous wave excitation source of the same transverse size as the input waveguide, placed at the output facet of the waveguide.

Received 25 April 2014; accepted 26 November 2014; published online 2 February 2015

References

1. Luk'yanchuk, B. *et al.* The Fano resonance in plasmonic nanostructures and metamaterials. *Nature Mater.* **9,** 707–715 (2010).
2. Chatterjee, R. *et al.* Achieving subdiffraction imaging through bound surface states in negative-refraction photonic crystals in the near-infrared range. *Phys. Rev. Lett.* **100,** 187401 (2008).
3. Kocaman, S. *et al.* Observations of zero-order bandgaps in negative-index photonic crystal superlattices at the near-infrared. *Phys. Rev. Lett.* **102,** 203905 (2009).
4. Veselago, V. G. The electrodynamics of substances with simultaneously negative values of ε and μ. *Usp. Fiz. Nauk* **92,** 517–526 (1964); *Sov. Phys. Usp.* **10**, 509 (1968).
5. Leonhardt, U. Optical conformal mapping. *Science* **312,** 1777–1780 (2006).
6. Pendry, J. B., Schurig, D. & Smith, D. R. Controlling electromagnetic fields. *Science* **312,** 1780–1782 (2006).
7. Rakich, P. T. *et al.* Achieving centimetre-scale supercollimation in a large-area two-dimensional photonic crystal. *Nature Mater.* **5,** 93–96 (2006).
8. Mocella, V. *et al.* Self-collimation of light over millimeter-scale distance in a quasi-zero-average-index metamaterial. *Phys. Rev. Lett.* **102,** 133902 (2009).
9. Arlandis, J. *et al.* Mesoscopic self-collimation and slow light in all-positive index layered photonic crystals. *Phys. Rev. Lett.* **108,** 037401 (2012).
10. Anderson, P. W. Absence of diffusion in certain random lattices. *Phys. Rev.* **109,** 1492–1505 (1958).
11. Schwartz, T., Bartal, G., Fishman, S. & Segev, M. Transport and Anderson localization in disordered two-dimensional photonic lattices. *Nature* **446,** 52–55 (2007).
12. John, S. Strong localization of photons in certain disordered dielectric superlattices. *Phys. Rev. Lett.* **58,** 2486–2489 (1987).
13. John, S. *Confined Electrons and Photons* Vol. 340, 523–584 (NATO ASI Series B, 1995).
14. Wang, J. & Genack, A. Z. Transport through modes in random media. *Nature* **471,** 345–348 (2011).
15. Levi, L., Krivolapov, Y., Fishman, S. & Segev, M. Hyper-transport of light and stochastic acceleration by evolving disorder. *Nature Phys.* **8,** 912–917 (2012).
16. Levi, L. *et al.* Disorder-enhanced transport in photonic quasicrystals. *Science* **332,** 1541–1544 (2011).
17. Burresi, M. *et al.* Weak localization of light in superdiffusive random systems. *Phys. Rev. Lett.* **108,** 110604 (2012).
18. Conti, C. & Fratalocchi, A. Dynamic light diffusion, three-dimensional Anderson localization and lasing in inverted opals. *Nature Phys.* **4,** 794–798 (2008).
19. Karbasi, S. *et al.* Image transport through a disordered optical fibre mediated by transverse Anderson localization. *Nature Commun.* **5,** 3362 (2014).
20. Asatryan, A. A. *et al.* Suppression of Anderson localization in disordered metamaterials. *Phys. Rev. Lett.* **99,** 193902 (2007).
21. De Raedt, H., Lagendijk, A. & de Vries, P. Transverse localization of light. *Phys. Rev. Lett.* **62,** 47–50 (1989).
22. Mott, N. F. *Metal–Insulator Transitions* (Taylor and Francis, 1974).
23. Lahini, Y. *et al.* Anderson localization and nonlinearity in one-dimensional disordered photonic lattices. *Phys. Rev. Lett.* **100,** 013906 (2008).
24. Savona, V. Electromagnetic modes of a disordered photonic crystal. *Phys. Rev. B* **83,** 085301 (2011).
25. Patterson, M. *et al.* Disorder-induced coherent scattering in slow-light photonic crystal waveguides. *Phys. Rev. Lett.* **102,** 253903 (2009).
26. Bliokh, Y. P., Freilikher, V. & Nori, F. Ballistic charge transport in graphene and light propagation in periodic dielectric structures with metamaterials: A comparative study. *Phys. Rev. B* **87,** 245134 (2013).
27. Ponomarenko, L. A. *et al.* Tunable metal–insulator transition in double-layer graphene heterostructures. *Nature Phys.* **7,** 958–961 (2011).
28. Esaki, L. & Tsu, R. Superlattice and negative differential conductivity in semiconductors. *IBM J. Res. Dev.* **14,** 61–65 (1970).
29. Ohtomo, A. & Hwang, H. Y. A high-mobility electron gas at the $LaAlO_3/SrTiO_3$ heterointerface. *Nature* **427,** 423–426 (2004).
30. Billy, J. *et al.* Direct observation of Anderson localization of matter waves in a controlled disorder. *Nature* **453,** 891–894 (2008).
31. Roati, G. *et al.* Anderson localization of a non-interacting Bose–Einstein condensate. *Nature* **453,** 895–898 (2008).
32. Carusotto, I. & Ciuti, C. Quantum fluids of light. *Rev. Mod. Phys.* **85,** 299–366 (2013).

Acknowledgements

We acknowledge discussions with M. Weinstein, S. Kocaman and C-T. Chen. We also thank S-N. Chiu for the data analysis. This work is supported by the Office of Naval Research under M. F. Shlesinger (N00014-14-1-0041) and the Studying Abroad Scholarship by the Department of Education in Taiwan. This work is also supported by NSF Division of Materials Research (1108176) and EPSRC EP/G030502/1. The electron-beam lithography carried out at the Brookhaven National Laboratory is supported by the US Department of Energy, Office of Basic Energy Sciences, under Contract No. DE-AC02-98CH10886. The authors acknowledge the use of the UCL Legion High Performance Computing Facility (Legion@UCL) and associated support services in the completion of this work.

Author contributions

P.H., N.C.P. and C.W.W. conceived the project. P.H. designed the photonic superlattices and performed numerical simulations, sample nanofabrication, measurements and image analysis. C.C. and M.L. performed the electron-beam lithography, and C.C. carried out focused ion beam imaging. J.F.M. performed the far-field and group velocity measurements. M.T. prepared the NSOM probes. N.C.P. designed the photonic superlattices and performed the theoretical analysis and FDTD numerical simulations. P.H., N.C.P. and C.W.W. wrote the manuscript, which all authors discussed.

Additional information

Supplementary information is available in the online version of the paper. Reprints and permissions information is available online at www.nature.com/reprints. Correspondence and requests for materials should be addressed to P.H., N.C.P. or C.W.W.

Competing financial interests

The authors declare no competing financial interests.

Supplementary Information for

Photon transport enhanced by transverse Anderson localization in disordered superlattices

P. Hsieh[1,2*], C. Chung[2,3], J. F. McMillan[1], M. Tsai[2,4], M. Lu[5], N. C. Panoiu[6,7], and C. W. Wong[1, 8*]

[1] Optical Nanostructures Laboratory, Center for Integrated Science and Engineering, Solid-State Science and Engineering, Mechanical Engineering, Columbia University, New York, NY 10027, USA

[2] Quantumstone Research Inc., Taipei 114, Taiwan

[3] Center for Micro/Nano Science and Technology and and Advanced Optoelectronic Technology Center, National Cheng Kung University, Tainan 701, Taiwan

[4] Center for Measurement Standards, Industrial Technology Research Institute, Hsinchu 300, Taiwan

[5] Center for Functional Nanomaterials, Brookhaven National Laboratory, Upton, NY 11973, USA

[6] Department of Electronic and Electrical Engineering, University College London, Torrington Place, London WC1E 7JE, UK

[7] Thomas Young Centre, London Centre for Nanotechnology, University College London, 17-19 Gordon Street, London, WC1H 0AH, UK

[8] Mesoscopic Optics and Quantum Electronics Laboratory, University of California, Los Angeles, CA 90095, USA

* Correspondence and requests for materials should be addressed to P.H., N.C.P or C.W.W. (email: ph2285@columbia.edu; n.panoiu@ucl.ac.uk; cheewei.wong@ucla.edu)

I. Schematic representation of a superlattice with 3 superperiods

A schematic representation of a photonic superlattice with 3 superperiods is shown in Figure S1. Superlattices consist of alternating layers of hexagonal photonic crystals (PhCs) and slabs of homogeneous material [SR1]. The hexagonal PhC and the photonic superlattice have different symmetry properties, and consequently they have different first Brillouin zones, as illustrated in Figure S1.

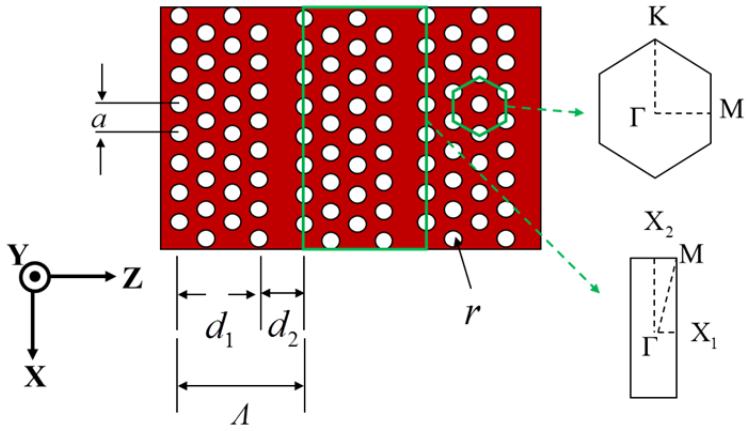

Figure S1 | Schematic representation of the photonic superlattice. First Brillouin zones for both the hexagonal photonic crystal lattice and photonic superlattices. a is the lattice period of the photonic crystal, r is the radius of the air holes, d_1 is the length of the photonic crystal layer, d_2 is the length of the homogeneous silicon slab, and $\Lambda = d_1 + d_2$ is the period of the photonic superlattice. In our design, the photonic crystal parameters are a = 500 nm, r/a = 0.29, $d_2/d_1 = 0.18$, and the silicon device thickness of the silicon-on-insulator wafer t = 320 nm. In all our fabricated devices, the PhC sections of the superlattice contain 7 lattice periods in the longitudinal direction (z-axis, which coincides with the Γ-M symmetry axis of the PhC).

II. Design of structural disorder and hole distribution in the superlattice

Structural disorder of the photonic superlattice is introduced by the perturbation of PhC holes with heptagonal, square, and triangular shapes. In particular, the scatterer (hole) shape is designed such that the circular hole coincides with the inscribed circle of the heptagonal and square scatterers, as shown in Figure S2.

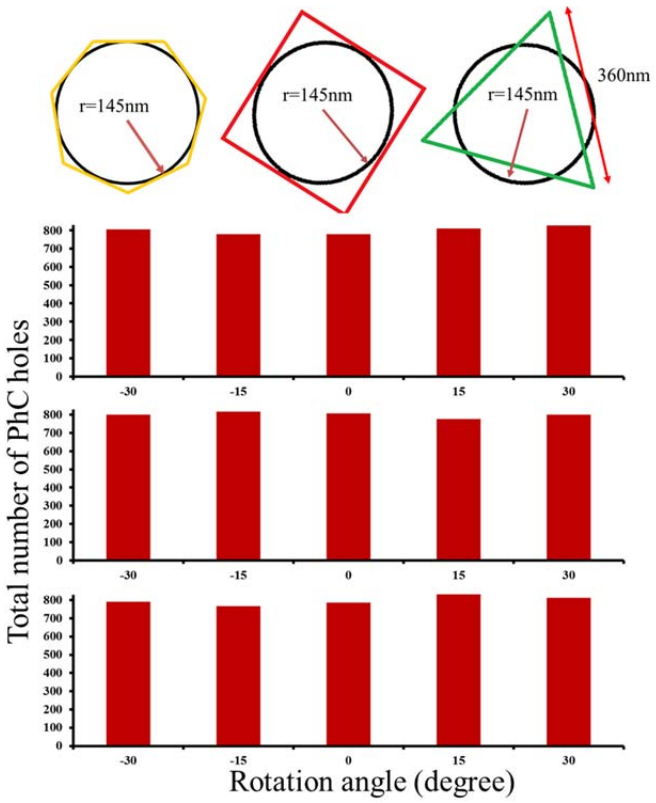

Figure S2 | Schematic representation of the disordered scatterers (top inset) and the stochastically-uniform distributions of the random rotations. From top to bottom, the panels correspond to the heptagonal-hole, square-hole, and triangular-hole superlattices.

For the triangular scatterer, we choose the edge size to be 360 nm for each side so that the area of the circular and the triangular holes are approximately equal. All the air hole scatterers are rotated by 0, 15°, -15°, 30°, or -30°, with the angle of rotation described by a stochastically-uniform random distribution. The distributions for the three families of scatterers are shown in Figure S2. The disorder distribution level is defined by the standard deviation of the total number of the rotation angles, which can be found as ~ 21.3°, ~ 21.2°, and -21.2° for the heptagonal-hole superlattice (HHS), square-hole superlattice (SHS), and triangular-hole superlattice (THS), respectively. We note that using a finite, discrete set of rotation angles is enough to introduce structural disorder in our photonic system. In Figure S3 we present the focused ion beam images of the resulting fabricated nanostructured superlattices (see Methods on nanofabrication parameters). In all cases the centers of the holes form a hexagonal lattice, within the positional accuracy of the electron-beam lithography writer.

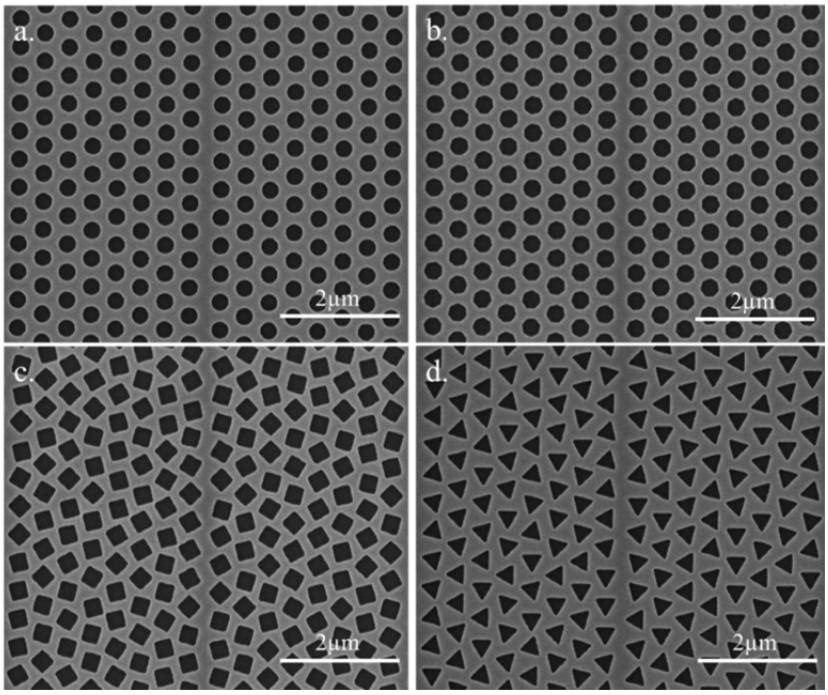

Figure S3 | Focus ion beam images of photonic crystal superlattices with different scatterer shape. a, circular-hole superlattice. **b,** heptagonal-hole superlattice. **c,** square-hole superlattice. **d,** triangular-hole superlattice.

An additional type of disorder is introduced if the size of the holes is set in the domain ($r-\Delta r/2$, $r+\Delta r/2$), where r is the radius of the circular hole, and Δr is the distance from each point on the boundary of the heptagonal, square, and triangular holes to the center of the circular hole. The level of structural disorder can then be further characterized by the averaged deviation of Δr from the circular hole radius r, averaged over 600 holes. Under these conditions, the structural disorder is determined to be ~ 2%, ~ 6%, and ~ 13% for the HHS, SHS, and THS, respectively.

III. Band diagrams, equifrequency surfaces, effective indices of refraction for the PhC and the homogeneous slab, and guiding resonances of the transverse PhC waveguides

The photonic band structures of the underlying PhC with hexagonal symmetry (see Figure S4a) as well as that of the photonic superlattice are computed by using RSoft's BandSOLVE, a commercially available software that implements a numerical algorithm based on the plane wave expansion of the electromagnetic field and spatial distribution of the dielectric constant of the photonic structure. For 1D approximations, cascaded 2×2 transmission matrices

through the PhC and the homogeneous regions can also be used. In all our three-dimensional (3D) numerical calculations of the photonic bands a convergence tolerance of 10^{-8} is enforced. The photonic bands of the PhC are classified based on their parity symmetry with respect to a plane crossing through the middle of the silicon slab, whose normal is along the *y*-axis, into TM-like (odd) and TE-like (even) modes. In particular, at the location of this plane the electric (magnetic) field of the TM-like (TE-like) mode is predominantly perpendicular onto the plane.

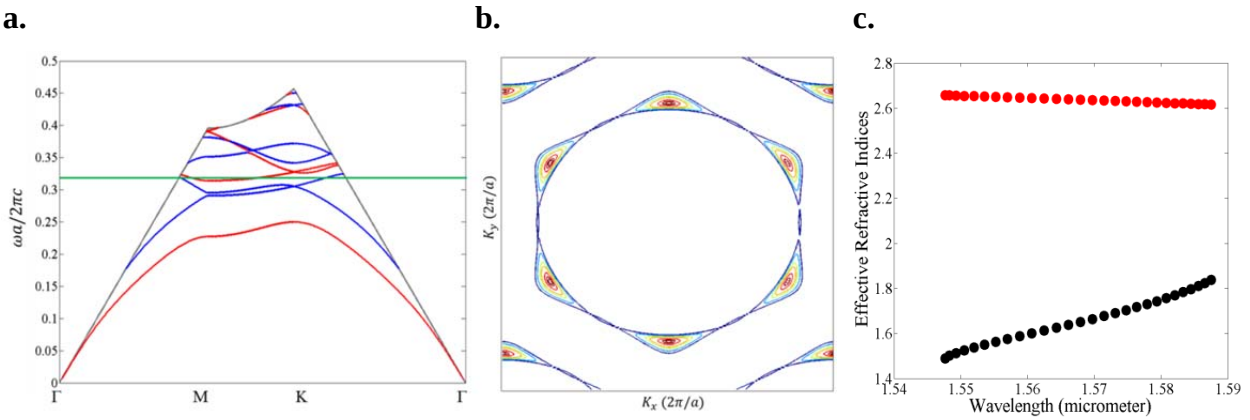

Figure S4 | Band structure, equifrequency curves, and effective mode refractive indices of the hexagonal photonic crystal. a, Guided mode band structure computed using a plane-wave expansion method, with the red (TE-like) and blue (TM-like) modes. The photonic crystal parameters are a = 500 nm, r = 145 nm, and t = 320 nm. **b,** Equifrequency curves of the photonic crystal. The weak anisotropy of the flat sections of the equifrequency curves leads to the observed collimation effect. **c,** Effective refractive indices of the second TM-like photonic crystal band (black) and the silicon slab (red), show all-positive refraction of the superlattice.

The equifrequency surfaces are determined from the band structure, and represent guided photonic modes of the PhC that correspond to a constant frequency. The equifrequency curves shown in Figure S4b illustrate that within a certain frequency range optical beams can only propagate in a narrow interval of angles, centered around the Γ-M direction. This weak anisotropy contributes to the observed collimation effect. The effective refractive indices corresponding to the second TM-like band (Figure S4c) are determined from the relation $k = \omega|n|/c$, with k in the first Brillouin zone.

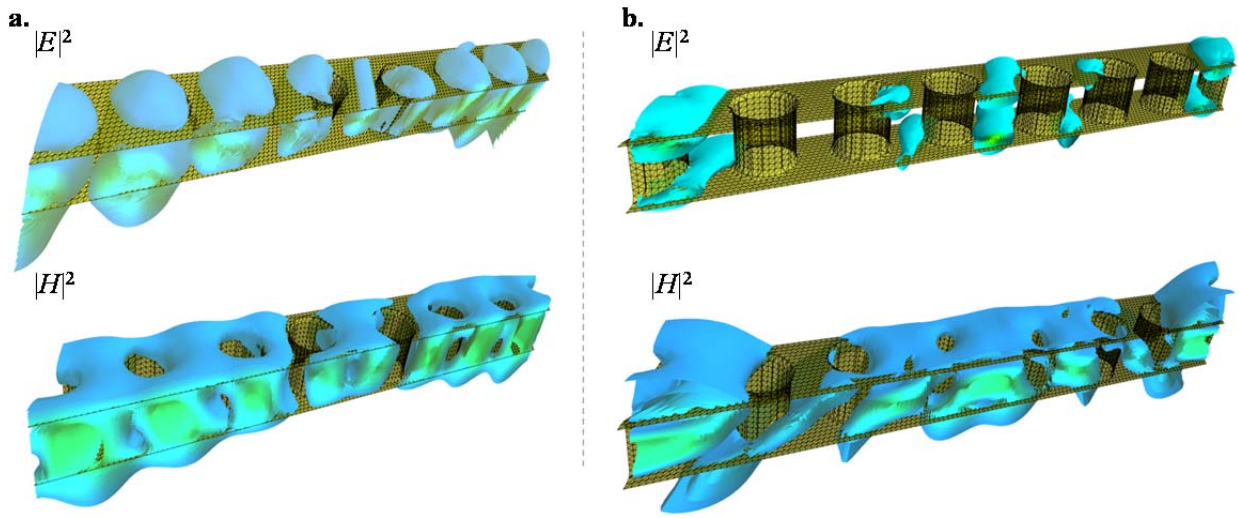

Figure S5 | $|E|^2$-field and $|H|^2$-field distributions of the guided modes of the photonic crystal superlattice, calculated at the Γ symmetry point. The modes correspond to a wavelength of 1529 nm (**a**) and 1590 nm (**b**). For a clearer visualization, the field profiles are presented as a set of isosurfaces corresponding to increasing values of $|E|^2$ and $|H|^2$. For clarity, the dielectric matrix of the photonic crystal is superimposed onto the field distributions

Figure S5 shows the computed spatial distribution of the electric field ($|E|^2$) and magnetic field ($|H|^2$) intensities of the guiding resonances (leaky modes) corresponding to the two flat bands (with normalized frequency near 0.314 and 0.327) illustrated in the zoomed-in band structure of Figure 1f in the main text. At the Γ symmetry point (k_x=0) these two modes are embedded in the radiation continuum of the PhC slab waveguide and represent guided resonances excited in the transverse 1D PhC waveguides.

IV. Finite difference time domain simulation and calculation of the effective beam width

The numerical simulations of the intensity field distribution have been performed with MEEP, a freely available code based on the finite-difference time-domain (FDTD) method [SR2]. In all numerical simulations we used a uniform computational grid of 33 grid points per micrometer. This choice ensures that the smallest characteristic length of the system (in our case, the diameter of the holes) contains at least 10 grid points, allowing sufficient numerical accuracy in all our cases concerning dielectric structures. In our numerical simulations we used a pulsed excitation source with a 1550 nm central wavelength with a spectral full-width half-maximum of 90 nm.

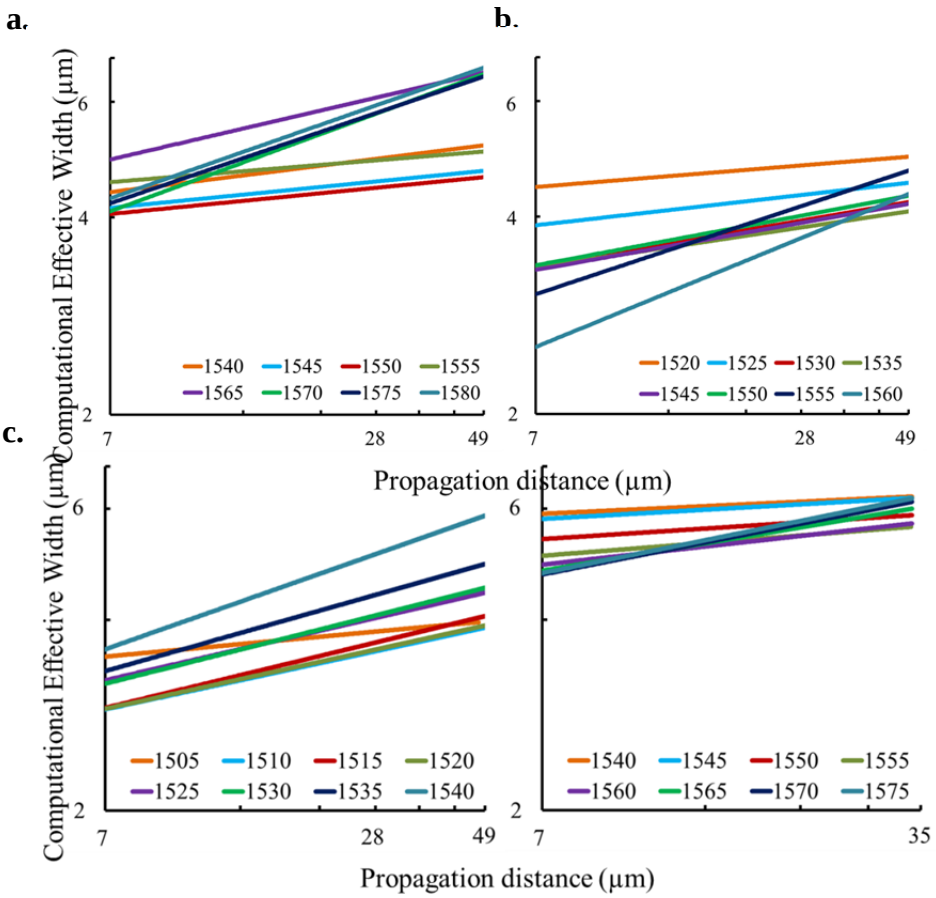

Figure S6 | Log-log plots of the simulated effective beam width versus the propagation distance. Summary for circular-hole superlattice (**a**), heptagonal-hole superlattice (b), square-hole superlattice (**c**), and triangular-hole superlattice (**d**).

The computed effective beam widths, $\omega_{effc}(z)$, for the different superlattice, propagation distance z, and wavelength, are summarized in Figure S6. The physical nature of the beam

divergence process is revealed by the slope of $\omega_{effc}(z)$ when represented in log-log scale. The log-log plot of the computationally determined beam width $\omega_{effc}(z)$ for the CHS shows the slope ν ~ 0.05 from 1545 nm to 1555 nm. In the presence of ~ 2% (HHS), ~ 6% (SHS), and ~ 13% (THS) disorder, the log-log plot of $\omega_{effc}(z)$ shows a significantly different spectral dependence of the slope ν (see main text).

In particular, for the HHS from 1525 nm to 1550 nm, ν ~ 0.05 to 0.1. For the SHS from 1505 nm to 1530 nm, ν ~ 0.05 to 0.1. For the THS from 1540 nm to 1575 nm, ν ~ 0.05 to 0.1. This illustrates that the collimation bandwidth increases when structural disorder is added to the system, in agreement with the experimental results described in the main text.

V. Analysis of the measured collimation and spatial full-width half-maximum in the periodic and disordered superlattices

Figures S7 to S10 represent several measured far-field infrared images related to the Figures 4d to 4g in the main text. Measurements are taken from 1530 nm to 1620 nm with 100 pm resolution, with hundreds of gigabytyes of data collected through a fast data acquisition card. The effects of laser speckle is also analyzed by averaging over 20 images, each taken at 1 pm spectral resolution apart, with no significant difference from the raw data below.

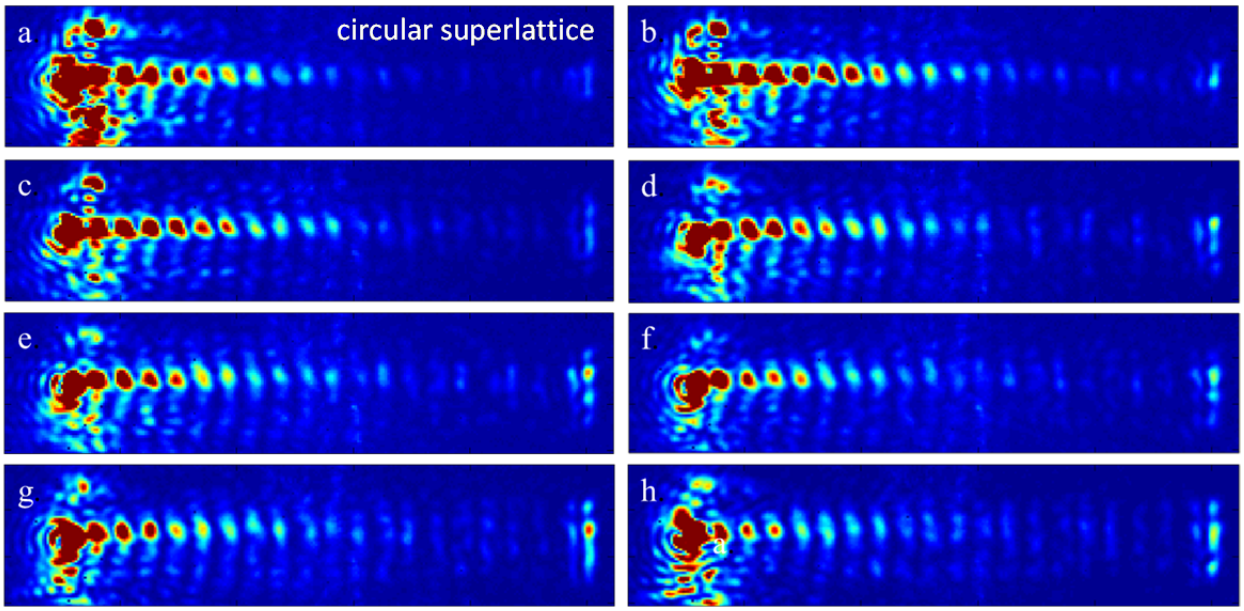

Figure S7 | Measured far-field infrared images of the circular-hole superlattice. a through **h,** at 1546 nm, 1550 nm, 1554 nm, 1558 nm, 1561 nm, 1564 nm, 1567 nm, and 1571 nm, respectively. Beam propagation is from left to right.

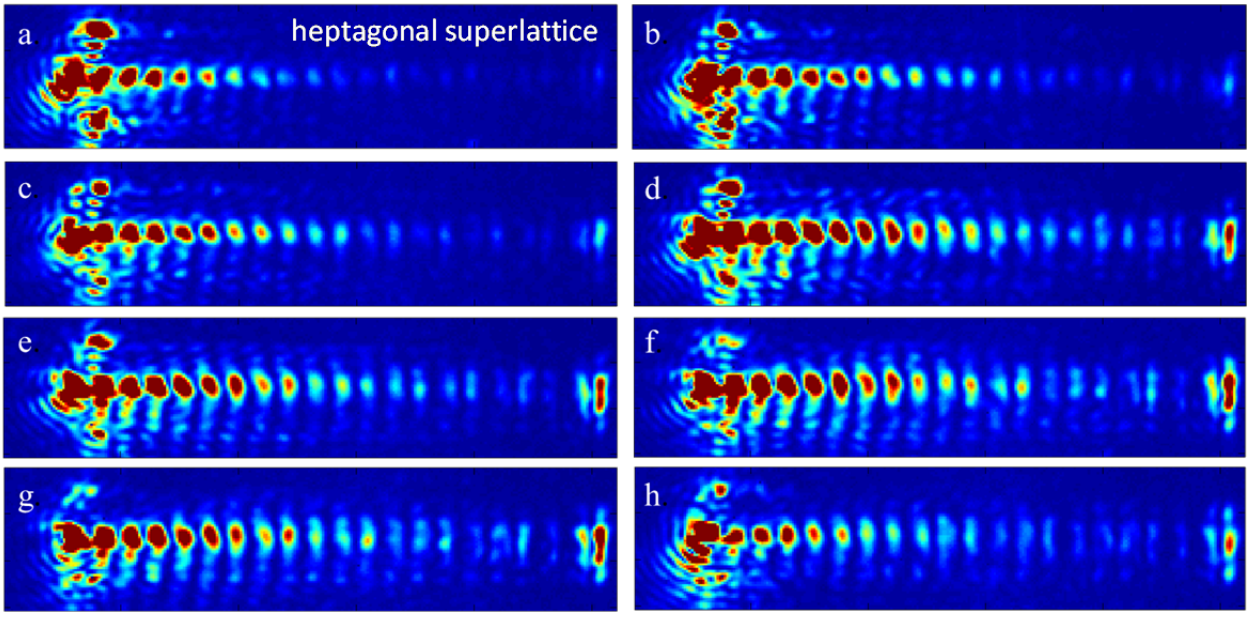

Figure S8 | Measured far-field infrared images of the heptagonal-hole superlattice. a through **h,** at 1546 nm, 1550 nm, 1554 nm, 1558 nm**,** 1561 nm, 1564 nm, 1567 nm, and 1571 nm, respectively. Beam propagation is from left to right.

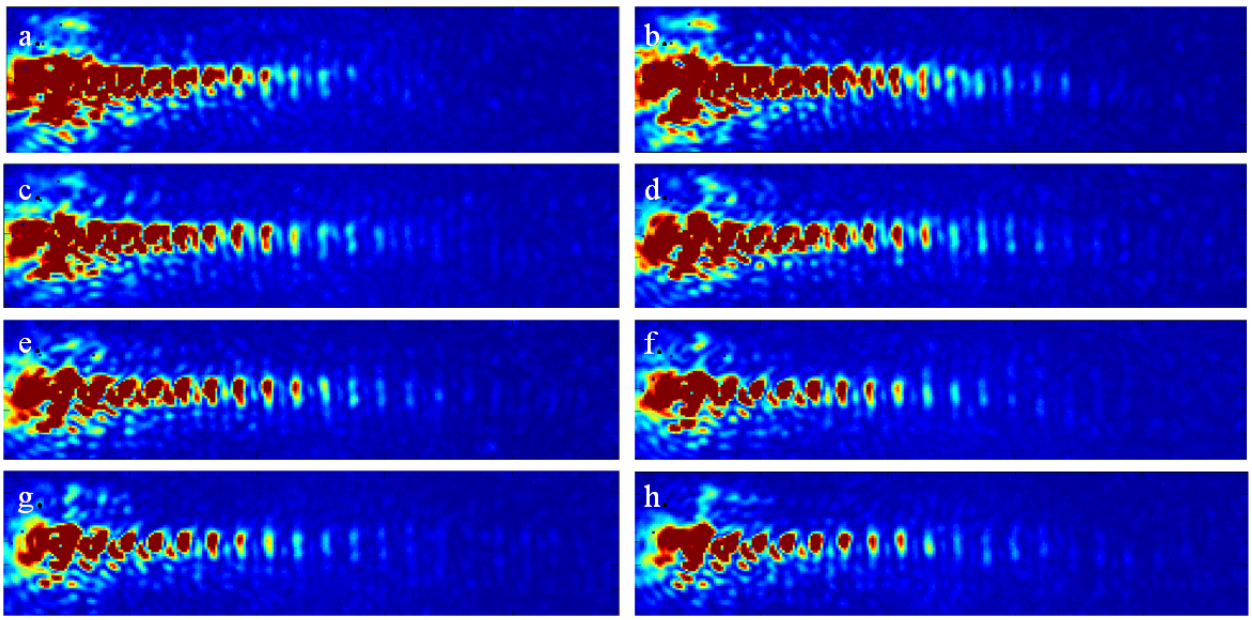

Figure S9 | Measured far-field infrared images of the square-hole superlattice. a through **h,** at 1551 nm, 1555 nm, 1559 nm, 1563 nm, 1566 nm, 1569 nm, 1572 nm, and 1576 nm, respectively. Beam propagation is from left to right.

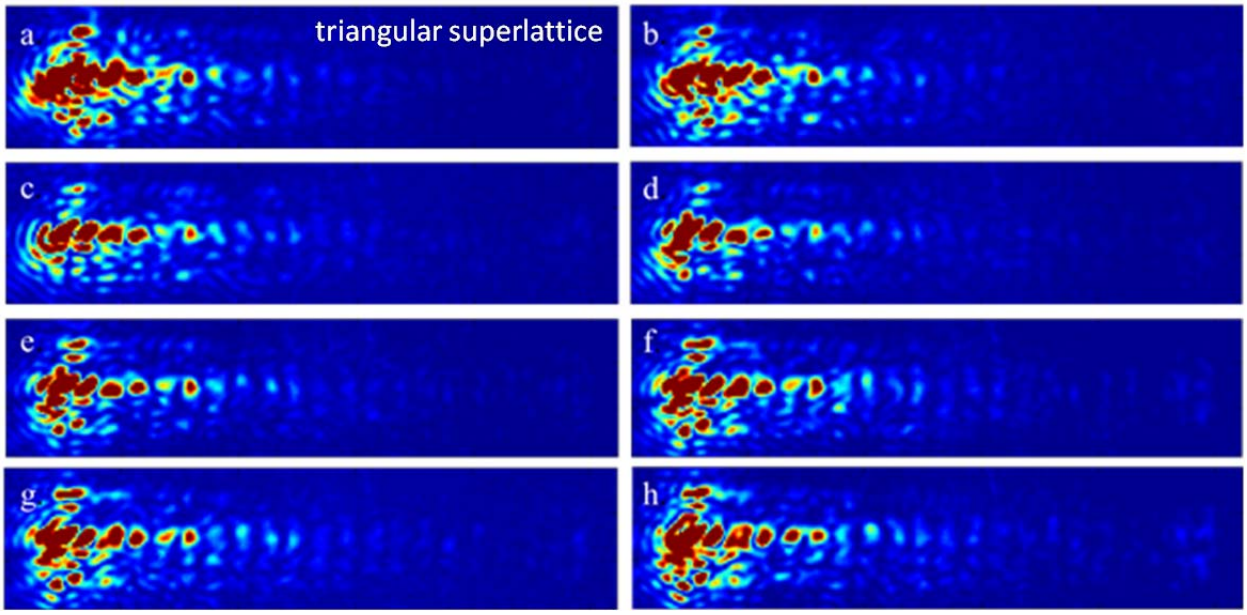

Figure S10 | Measured far-field infrared images of the triangular-hole superlattice. a through **h,** at 1576 nm, 1580 nm, 1584 nm, 1588 nm, 1591 nm, 1594 nm, 1597 nm, and 1601 nm, respectively. Beam propagation is from left to right.

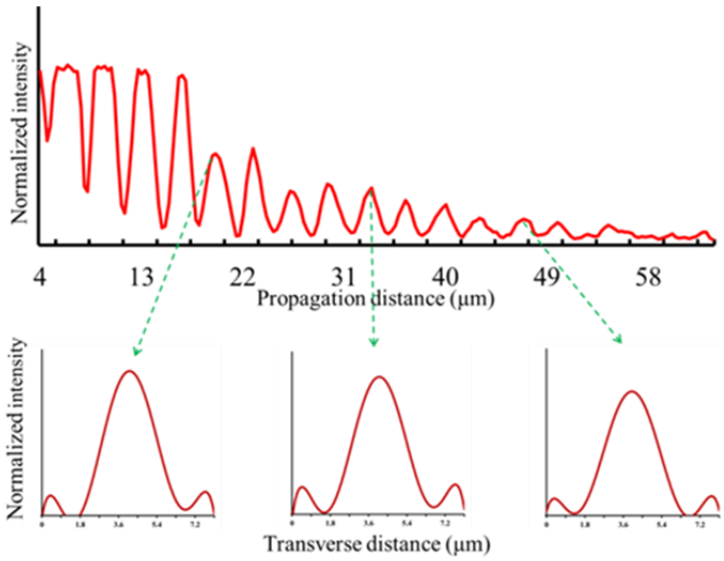

Figure S11| Intensity distribution along the propagation distance (*z*-axis) at 1550 nm. The top plot shows the *z*-dependence of the intensity distribution for the circular-hole superlattice, whereas examples of the intensity distribution along the transverse distance (*x*-axis), at several locations along the *z*-axis, are presented in the bottom panels.

The full-width at half-maximum (FWHM) of the collimating beams are determined at all maxima intensity locations along the superlattice, as shown in Figure S11 (circular superlattice shown). For the disordered superlattices (HHS, SHS, and THS), the transverse spatial profile is best matched with an exponential decay instead of a Gaussian profile, further supporting the evidence of transverse localization. Next, the beam FWHM versus the propagation distance is represented on log-log scale and linear fitting is used to determined the corresponding slope, as per Figures 4d to 4g in the main text. More specifically, from the asymptotic dependence of the beam width it is found that ω_{FWHM} is of the form $\omega_{FWHM}(z) \propto z^{\nu}$, where ν is a power exponent whose value was calculated to be in the range ν<0.5. This is compared to the calculated effective width versus propagation distance determined from FDTD simulations in Figure S6.

In addition, the collimating beam profile shows transverse symmetry as per Figure S12, from both the numerical simulations and measurements. From the 3D simulations, with increasing disorder the transverse asymmetry is larger. The beam profile asymmetry is observed in the measurements as well, with several examples presented here. Note that the measurements and simulations correspond to different structural disorder realizations and therefore the particular field profiles should not be directly compared.

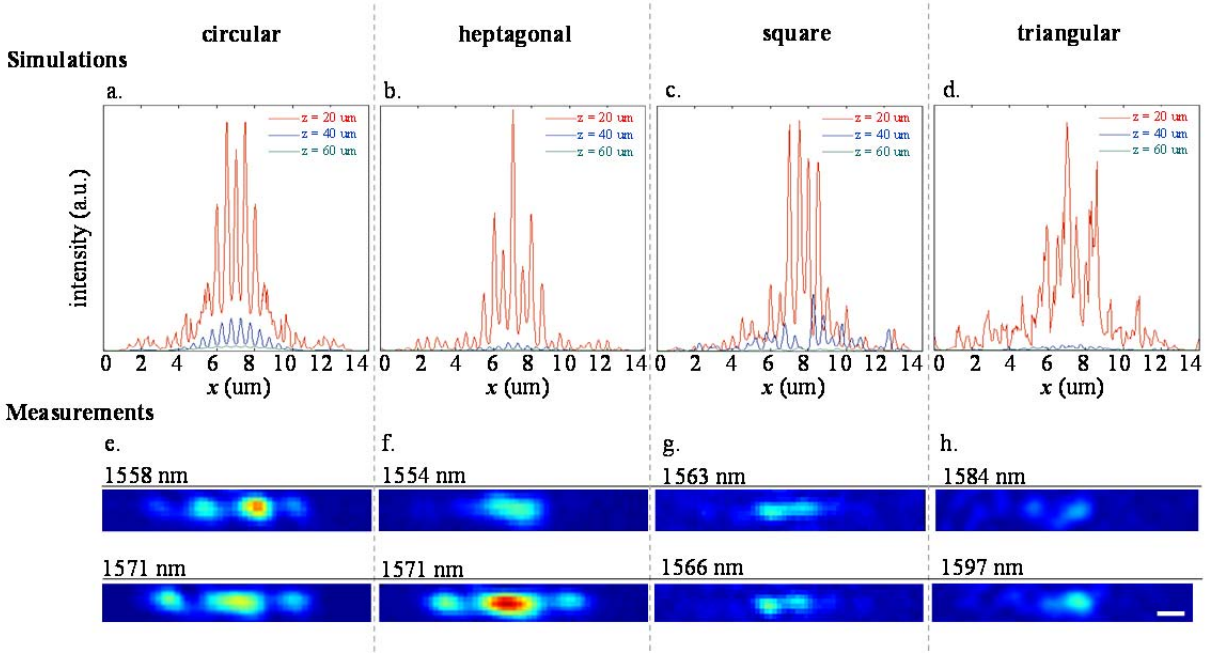

Figure S12 | Asymmetric transverse beam profiles for the CHS, HHS, SHS and THS superlattices, determined both from the numerical simulations and measurements. In the simulations, the wavelengths are 1550 nm (CHS), 1530 nm (HHS), 1515 nm (SHS), and 1550

nm (THS), and correspond to the maximum observed collimation. In the measurements, the example wavelengths are indicated at the top left of the panels, each taken at the output or near the output. Scale bar: 2 μm.

VI. Near-field scattering imaging finer feature of collimation:

The near-field scanning optical microscope used to examine the optical near-field is a Veeco Aurora-3, a commercial and aperture-type near-field scanning optical microscope.

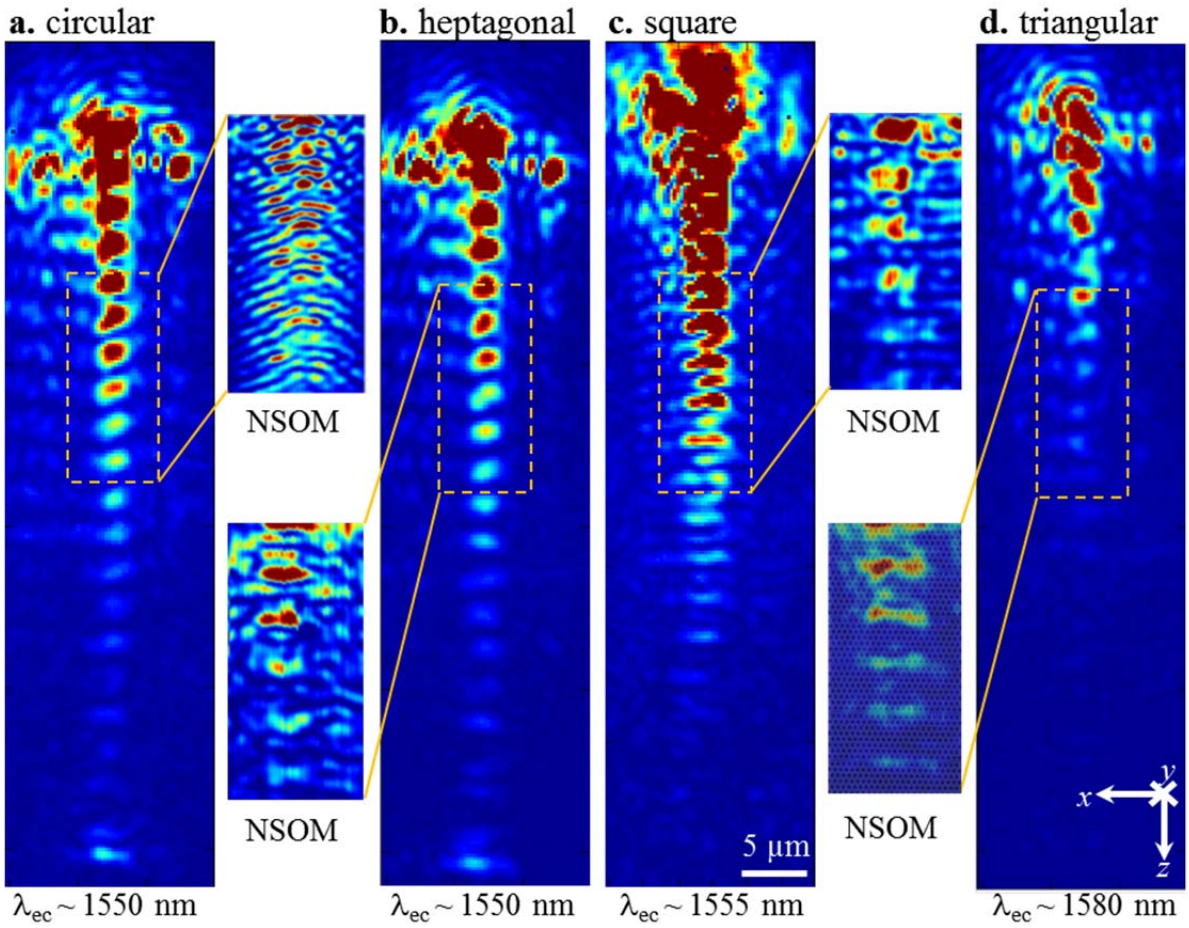

Figure S13 | Far- and near-field infrared scattering images illustrating the wavelength dependent beam collimation. a, Circular-hole superlattice at 1550 nm. **b,** heptagonal-hole superlattice at 1550 nm. **c,** square-hole superlattice at 1555 nm. **d,** triangular-hole superlattice at 1580 nm. The primary image represents the far-field, with the zoomed insets being extracted from the near-field scanning optical microscopy images.

The near-field probe was produced by using of thermal pulling method to create ~ 150 nm apertures and the tip was coated with a 100 nm aluminum layer for light confinement. The near-field probe was then attached to a tuning fork sensor produced by Veeco Instruments/Bruker AFM for constant-distance scanning. The piezoelectric scanner of near-field scanning optical microscope was calibrated by a periodic grid sample in topography image mode to ensure the accuracy of the measurements. To couple light into the optical chip, a UV-curing adhesive was used to bond a tapered lens fiber to the silicon input waveguide, with stable attachment. Beam propagation through the superlattices was observed with the near-field microscope and the Santec TSL-510 tunable laser used to obtain the spectral character. Detection was performed with a New Focus 2153 InGaAs femtowatt photoreceiver with ~ 23 fW/Hz1/2 noise equivalent power.

VII. Disordered anisotropic medium with flat spatial dispersion curves

In order to investigate the transverse light localization in the superlattice, we also nanofabricated and examined a set of anisotropic artificial mediums, with the collimation mechanism of flat spatial dispersion surfaces studied in earlier works (Refs. 6-8 in main text). These anisotropic artificial media were based on a square lattice design, with the device size of a few hundred micrometers. The PhC hole-to-lattice ratio r/a =0.305, with lattice period a= 360 nm. Figure S14a shows equifrequency curves for the second TE band of the PhC, with the relevant contours near the wavelengths of interest. For the normalized frequency ω=0.2236, whose equifrequency curve is represented in Fig. S14 by the red contour, the PhC shows remarkably small spatial dispersion (weak anisotropy), which suggests beam collimation. This wavelength, at which the collimation is most effective, is denoted by λ_{ec}.

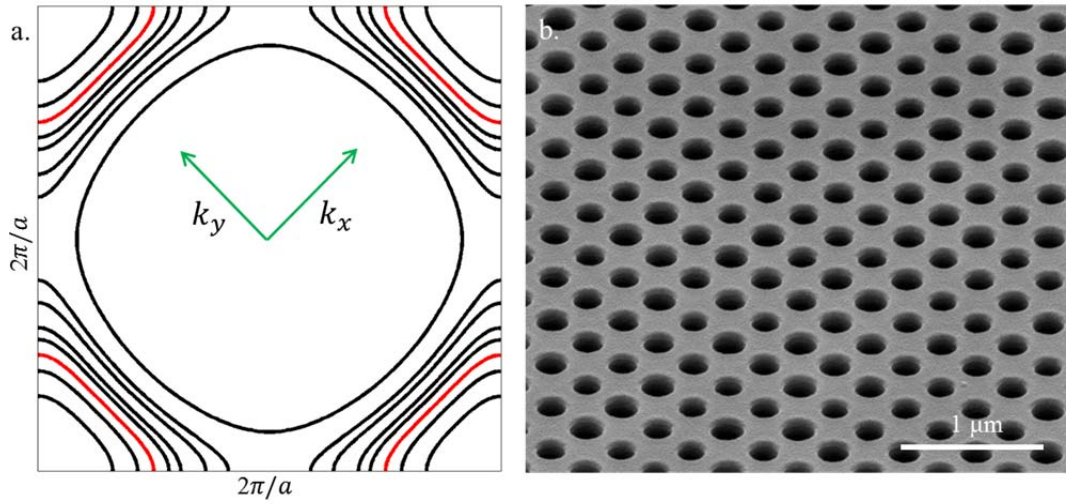

Figure S14 | Photonic crystals as anisotropic media. a, computed equifrequency surface of the periodic photonic crystals. Red curves correspond to the normalized frequency ω=0.2236, which leads to most effective collimation. **b,** example of nanofabricated photonic crystal with highest level of disorder, imaged through focused ion beam.

To introduce disorder in this photonic system, three other disordered structures were also designed and fabricated, with different levels of perturbation of the PhC holes. For each level of disorder, the radius of the hole was described by a uniform random distribution with different width. The three layouts of disordered PhC were subsequently generated by using these random distribution functions and prepared for fabrication. The lattice period of all the disordered PhC was the same, a=360 nm, so as a reliable comparison of the beam propagation in the PhCs can be made. Figure S15 shows the radius distribution corresponding to the three levels of disorder, from the lowest (Fig. S15a) to the highest (Fig. S15c) disorder level.

Using the method described in main text, the cleaved nanofabricated chip was mounted on the sample holder. Then a TE-polarized optical beam was coupled into the PhC via a focus lens, this process being repeated 10 times. In each of these 10 measurements, the coupling point was randomly shifted in the horizontal direction of the device, to ensure that the results are not dependent on a specific termination profile of the PhC.

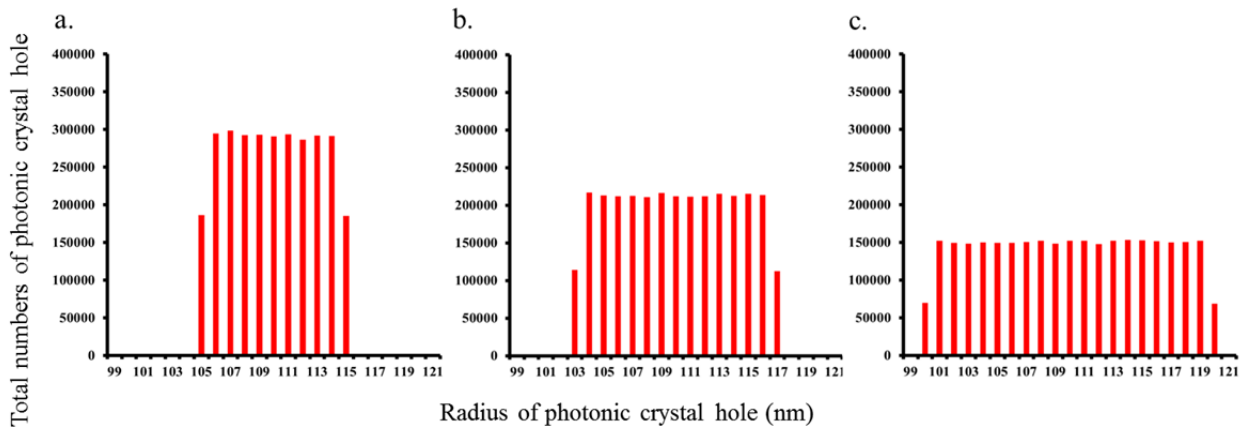

Figure S15 | Distribution of the hole radius for different levels of disorder in a PhC based anisotropic medium. a, low level of disorder. **b**, medium level of disorder. **c**, high level of disorder.

VIII. Transmission spectrum and group-velocity delay further evidencing the relation between the excitation of transverse guided modes and the observed collimation

Furthermore we performed group velocity delay and transmission spectra measurements of the superlattices. For the precision amplitude and phase measurements, coherent swept wavelength interferometry is implemented, with 500 fm wavelength precision and time delays of up to a few nanoseconds.

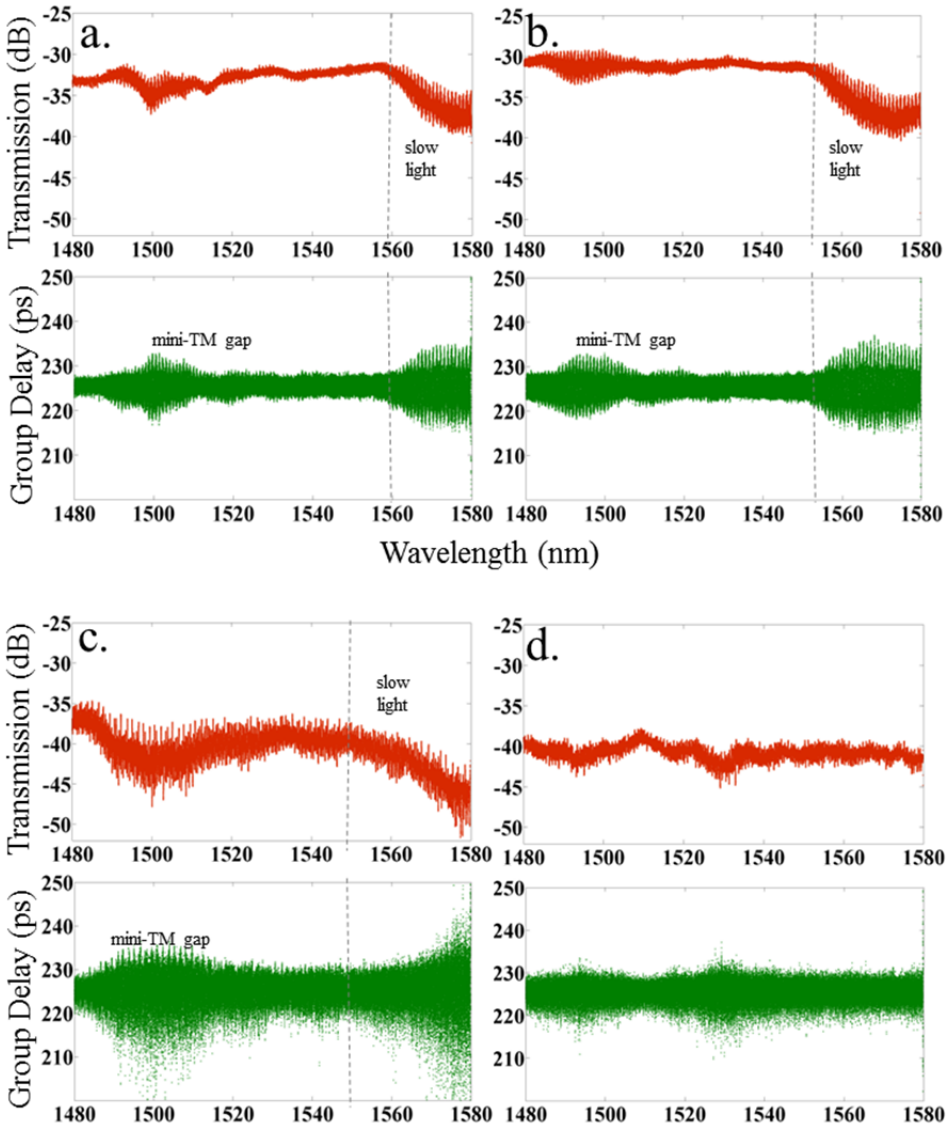

Figure S16 | Transmission spectra and group velocity delay of the circular-hole superlattice (**a**), with slow-light regime for wavelengths larger than ~ 1560 nm. A mini-transverse-magnetic gap around 1500 nm arises from the higher-order modes. **b,** heptagonal-hole, **c,** square-hole, and **d,** triangular-hole superlattice.

The interferometry is performed in a dual-stage fiber interferometer with absolute hydrogen cyanide $H^{13}C^{14}N$ gas cell reference of the $2\nu_3$ rotational-vibrational absorption lines, with optimized power in the local oscillator. We also note that the group-delay measurements are taken relative to an input delay, a constant value of which is uniformly used for all superlattices for comparison. Shorter superlattices (of 5 superperiods) are also used in the transmission measurements to provide sufficient transmission signal for accurate measurements, as shown in

Figure S13. The transmission spectrum and group velocity delay of each device are measured experimentally within the spectral range of 1480 nm to 1580 nm.

Slow-light band edges are observed to occur concurrently near the wavelengths of most effective collimation λ_{ec}, and away from the higher-order transverse-magnetic mini-gap around 1500 nm. In the regular CHS superlattices, this slow-wave propagation arises due to *z*-cascaded evanescently coupled transverse guided modes, further evidencing the relation between the transverse guided mode excitation and the observed CHS collimation.

Supplementary References:

[SR1] Kocaman, S., Aras, M. S., Hsieh, P., McMillan, J. F., Biris, C. G., Panoiu, N. C., Yu, M. B., Kwong, D. L., Stein, A., & Wong, C. W. Zero phase delay in negative-refractive-index photonic crystal superlattices. *Nature Photonics* **5**, 499 (2011).

[SR2] Oskooi, A. F., Roundy, D., Ibanescu, M., Bermel, P., Joannopoulos, J. D., & Johnson, S. G. MEEP: A flexible free-software package for electromagnetic simulations by the FDTD method, *Computer Physics Communications* **181**, 687 (2010).